Multiparameter Optimization of Microbial Fuel Cell Outputs Using Linear Sweep Voltammetry and Microfluidics

Jayesh M. Sonawane[1] and Jesse Greener[1,2*]

[1]Département de Chimie, Faculté des sciences et de génie,
Université Laval, Québec City, QC, Canada

[2]CHU de Québec, Centre de recherche, Université Laval,
10 rue de l'Espinay, Québec, QC, Canada
* Corresponding author: jesse.greener@chm.ulaval.ca

Graphical abstract

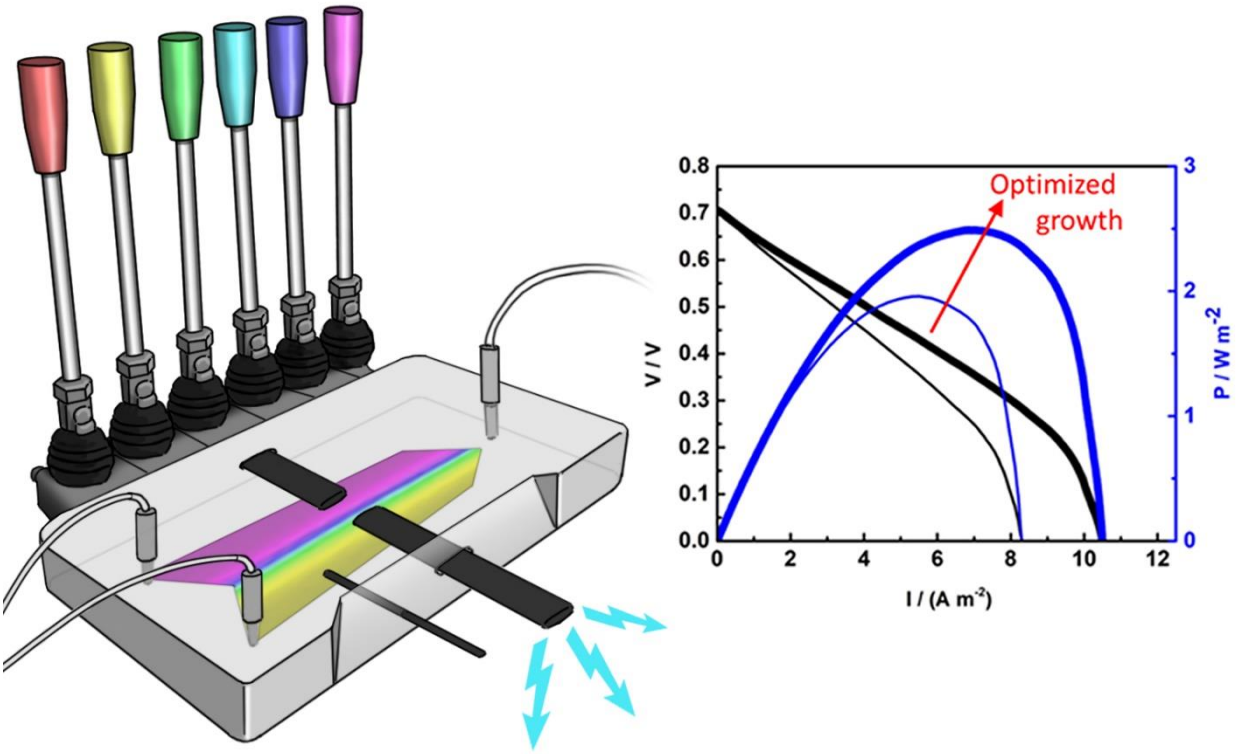

Abstract

A microbial fuel cell with a pure-culture *Geobacter sulfurreducens* electroactive biofilm was used for performance optimization by making rapid changes to experimental parameters in microchannels while monitoring their effect using linear sweep voltammetry. A systematic investigation of polarization behavior and evaluation of system resistivity provided important figures of merit and mechanistic insights on the effects of flow rates, concentrations, and temperature after reaching maturity. After individual parameters were optimized, a synergistic effect was observed by applying optimal parameters together, resulting in improved current and maximum power densities, compared to stable values at unoptimized conditions. Continued acclimation for just two days under these conditions resulted in further improvements to anode area-normalized current and power maxima (10.49±0.23 A m^{-2} and 2.48±0.27 W m^{-2}), which are among the highest reported in the literature for a microfluidic MFC. In keeping with other accepted normalization protocol using the area separating anode and cathode chambers, the outputs were recalculated as 64 A m^{-2} and 15 W m^{-2}.

Keywords

Microfluidics, microbial fuel cells, high-throughput optimization, polarization curve, current density, power density, linear sweep voltammetry, *Geobacter sulfurreducens*.

1. Introduction

Microbial fuel cells (MFCs) are bioelectrochemical devices that convert chemical energy into electrical energy by incorporating the oxidation of organic molecules into the metabolic pathways of certain electrogenic bacterial species. These bacteria can form electroactive biofilms (EABs) [1,2] on electrode surfaces, which usually serves as an electron sink from which an external electrical circuit can be powered. Wastewater treatment is one of the most important target applications for MFCs, largely because the process is anaerobic, which can significantly reduce energy costs compared to modern wastewater installations that require aeration. In wastewater conversion applications, high current is sought due to its direct relation to the molecular oxidation rate. Development of MFCs is typically conducted at the sub-liter scale in either batch or flow mode. At the same time, high power is desired to help offset power requirements for wastewater treatment processes and even to generate surplus power.

Emerging trends toward microfluidic MFCs have been boosted by recent technical advancements, such as the use of standard graphite electrodes and the protection of EABs from oxygen or other electron acceptors. Additionally, wastewater treatment has been demonstrated using an increasing number of substrate molecules, thus opening the door to implications for a large range of potential industries [3]. Microfluidics is becoming a new option for study and development of MFCs, with results that are transferable to prevailing larger-scale systems [4,5]. Especially important is that they are flow-based and can, thus, maintain concentration conditions due to constant replenishment of nutrient liquids [4,6]. Thanks to the ability to change experimental conditions precisely and instantaneously, microfluidic MFCs are ideal for the rapid optimization of experimental parameters, in contrast to macroscale batch reactors, which require multiple fill-refill cycles to evaluate even a single operational variable at time scales sufficient for EAB stabilization. Several operating parameters play a crucial role in MFC performance, including flow and other hydrodynamic parameters [7], types and concentrations of buffer molecules [8], substrate

molecules [3,9,10], terminal electron acceptors [11,12], biofilm age, and operating temperature [13–17]. Therefore, an effective optimization routine requires many experiments that can explore the wide reaction variable space and confirm predictions from simulations [18]. Due in part to a complete lack of turbulence, microfluidic MFCs are especially accurate in setting experimental conditions, making them well-suited for system optimization [1,4] of parameters related to hydrodynamic properties (shear stress, pressure chemical gradients, nutrient availability) [19–21]. As well, low thermal mass enables unparalleled control over setting and maintaining thermal conditions with minimal spatial variations [22]. Thus, microfluidic control coupled with the same electrochemical measurement techniques that are available to study bulk-scale MFCs [23] opens the door to a class of powerful platforms for optimization and discovery for MFCs [24], as well as three-electrode bioelectrochemical devices that are capable of performing more advanced experimental techniques [25,26]. One such technique is linear sweep voltammetry (LSV) because it is simple and informative, enabling characterizing of a wide range of macro- or microscale cell properties, including open circuit potentials, system resistances, and power and current densities [8,27–29].

In this work, we optimized individual experimental parameters using LSV to characterize and study the outputs from a microfluidic MFC containing pure-culture *G. sulfurreducens* while the flow rates, concentrations, and temperatures were controlled. From these studies, we obtained power density, current density, and cell resistances in the ohmic and diffusion-limited regions of the polarization curves. The synergetic effect of all of the individually optimized parameters led to immediate improvement, marked by high maximum current and power densities (5.50±0.74 A m^{-2} and 1.95 ±0.15 W m^{-2}, respectively). Finally, after acclimation to optimized conditions for just two days, the system rapidly adjusted its performance, reaching maximum outputs of 10.49±0.23 A m^{-2} and 2.48±0.27 W m^{-2}, which are among the best values reported in the literature for microfluidic MFCs. For comparison with other work that normalizes outputs by the cross-sectional area between electrodes rather than electrode area, we found that current and power densities in this work are 64 A m^{-2} and 15 W m^{-2}.

2 Materials and methods

2.1 Device fabrication

2.1.1 Mold fabrication

A photomask was designed using AutoCAD and printed using a photoplotter (FPS25000, Fortex Engineering Ltd., UK). A negative p33olarity photoresist film (Sandro Baumgart, MungoLux, Kümmersbruck, Germany) was laminated to a 1-mm-thick glass slide using a dry film laminator (FL-0304-01, Fortex Engineering Ltd., UK) operating at 70^{o}C, resulting in a final thickness of 160 µm. The photomask was placed on top of the glass/photoresist assembly and loaded into a UV exposure system (AY-315, Fortex Engineering Ltd., UK). The UV light that passed through the transparent regions of the mask resulted in cross-linking of the photoresist. Afterward, the uncross-linked photoresist was removed using developer and rinse solutions (SY300 Developer/Rinse, Fortex Engineering Ltd., UK). The final mold had the inverse features of the microchannel, upon which the electrodes were placed during device fabrication to achieve their integration at the bottom of a polydimethylsiloxane (PDMS) channel.

2.1.2 Electrode integration and device preparation

The present microfluidic MFC had electrodes positioned in the popular side-by-side orientation [30]. However, to best discriminate between results using different applied chemical concentrations and hydrodynamic conditions, it was previously predicted that the electrodes should be placed away from the channel corners to avoid large differences in flow velocities and ohmic resistance compared to other positions on the electrode closer to the opposite electrode [31]. Thus, in this study, the electrodes were placed 1 mm away from the vertical channel walls, as shown in Figure 1a, using a newly developed bridge-type electrode, as shown in the diagram cross-section in Figure 1b. In this approach, the electrodes were fixed to a specific portion of the channel feature on the mold before pouring the liquid PDMS and cross-linking agent Sylgard184 (Dow sylgard™ 184, Ellsworth Adhesives, Canada) around the entire assembly. Fixation was achieved using water-soluble polyvinyl acetate glue (Glue-all, Elmer's, Canada) so that no PDMS could penetrate between the mold and the electrode surface before solidification. The glue was selected because it could be easily released with the aid of a thin blade and washed away following demolding. To level the electrode against the channel feature on the mold, a ca. 300-µm-thick layer of PDMS was added to the bottom of the glass mold. The final dimensions of each electrode in contact with the liquid contents in the microchannel was 10 × 3 mm, with an interelectrode spacing

of 4.5 mm from edge to edge. It should be noted that this placement is closer than that of other microfluidic MFCs produced in our group, which usually measure 6 mm between electrodes.

Additional details on the preparation of the microfluidic MFC have been presented previously [4], but we note in passing that anerobic conditions were established on-chip by completely coating all exposed PDMS with epoxy, and the perfluoroalkoxy connective tubing (PFA tube 1/16, Hamilton Inc., Canada) was covered in a layer of gas-impermeable tape (Loctite 249 Anaerobic Blue Threadlocker Tape, Medium Strength, Henkel Corp., Mississauga, Canada) before a coating of epoxy was applied.

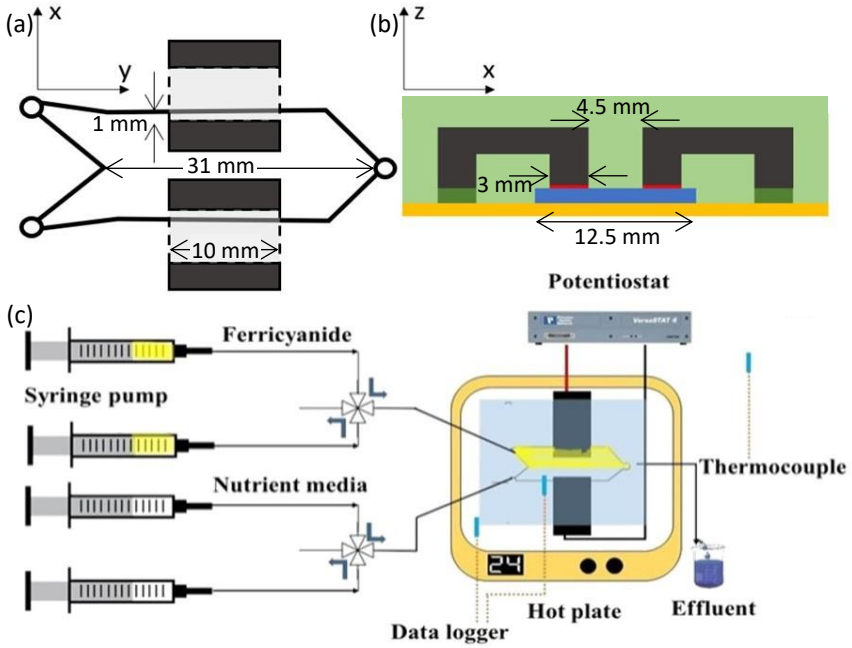

Figure 1. Microfluidic MFC device from a bird's eye view (a) and cross-sectional view (b) with dimensions indicated. The total downstream length of 31 mm is measured from the upstream intersection of the inlet channels and the outlet and width of 12.5 mm. The anodes and cathodes (black) within the device are constructed using solid graphite and each measures 10 mm in length and 3 mm in width. The separation between the anode and cathode within the device is precisely 4.5 mm. (a) Schematic of the channel with graphite electrodes placed 1 mm away from the channel wall. The electrode portion outside of the channel was used to make the connection to the potentiostat. (b) Cross-section of the bridge electrodes embedded in PDMS (green) atop the mold glass support (yellow)/photoresist (blue) mold. The in-channel electrode portion was reversibly glued to the stick-on mold channel feature with PVA glue. A spacer (dark green) between the glass and the out-of-channel electrode portion was used to level the electrode vis-à-vis the channel/electrode contact and filled with PDMS. (b) Device after curing of PDMS for 6 hours. (c) Schematic of the experimental setup with anolyte and catholyte fluid delivery using two 4-way valves, a hot plate with multiple thermocouples, and connection to a potentiostat.

2.2 Biological preparation and MFC operation

Geobacter sulfurreducens in a nutrient medium, with 40 mM sodium fumarate as a soluble electron acceptor, was used as an inoculum. The growth medium was composed of 10 mM sodium acetate (unless otherwise indicated) in a sodium phosphate buffer (3.8 mM NaH_2PO_4, 30 mM $NaHCO_3$, 1.3 mM KCl, 28 mM NH_4Cl) with 50 µg mL^{-1} of spectinomycin. No oxygen scavengers were used in this work. The microfluidic MFC was inoculated by injecting fumarate containing *G. sulfurreducens* into the microchannel using a 30 mL glass-tight syringe at a flow rate of Q=0.5 mL h^{-1} for 6 h. A co-flowing stream of ferricyanide (30 mM, unless otherwise noted) solution in a phosphate buffer (Q=0.5 mL h^{-1}) was admitted into the channel as the catholyte during inoculation. The phosphate buffer solution with a pH of 7 was prepared by mixing 2.290 g L^{-1} of Na_2HPO_4 and 2.256 g L^{-1} of NaH_2PO_4 to obtain a final concentration of 30 mM. Both the anolyte and catholyte inlets were connected to a 4-way valve for easy exchange of syringes without interruption [5]. After inoculation, the anolyte was switched to a sterile acetate solution (with no fumarate), and both solutions flowed from 50 mL gas-tight syringes at Q=0.5 mL h^{-1}, with total flow rate Q_T=1 mL h^{-1}, which was the default flow rate unless stated otherwise. The use of 4-way valves has been demonstrated previously as a key feature that ensures continuous bubble-free liquid delivery to a microfluidic MFC.

2.3 Analytical methods and calculations

At the beginning of the experiment, the electrodes were connected across a 100 kΩ external resistor, and the voltage drop (V) across it was recorded. Current (j) was calculated by Ohm's law: j=V/R. The raw current and raw power (P) were normalized by area (Eqn. 1):

$$j0=j/A \quad \text{(Eqn. 1a)}$$

$$P0=P/A \quad \text{(Eqn. 1b)}$$

where A is the normalization constant (m^2), and j0 and P0 are the normalized current and power, respectively. Two normalization methods were used featuring different normalization constants. The first normalization constant was the projected anode surface area, which accounts for limitations from available surface area for EAB colonization. In the present case, this was using the 10 mm × 3 mm anode (A_{anode} =3×10^{-5} m^2). The second method used the cross-sectional area

between the anode and cathode compartments to account for limitations in the electrolyte current pathways, which has been demonstrated in typical benchtop MFCs [32,33] and microfluidic MFCs [4]. In the present case, this cross-section normalization area was 31 mm × 0.16 mm ($A_{x\text{-}sect}$= 5×10^{-6} m^2). All electrochemical experiments were conducted using a potentiostat (Squidstat plus, Admiral Instruments, United States). Polarization curves were obtained using linear sweep voltammetry (LSV) recorded at a scan rate of 1 mV s^{-1} in a potential window from open circuit voltage (OCV) to 0 V. This scan rate was determined to be adequately slow to avoid distortions in the polarization and power density curves [34,35], but fast enough to ensure that the EAB was at a pseudo-static growth state (3 hours). Polarization curves were converted to power density curves using Equation 2:

$$P0=V^2/(R\times A) \qquad \text{(Eqn. 2)}$$

where R is the external resistance. Both Ohm's law and Equation 2 reveal that current and power are inversely related to external resistance. At the maximum power point, where $P0=P0_{max}$, the internal and external resistances are equal, and maximum power is directly proportional to the internal resistance [36]. Unless otherwise stated, all LSV tests were run in triplicate, and the values extracted from polarization and power density curves represent their averages, with error bars displaying the standard deviation in the results.

In this work, we analyzed the polarization and power density curves produced from LSV under the various experimental conditions. Based on Ohm's law, the relationship between potential and current in the polarization (IV) curve was exploited to reveal details about the internal resistance. We systematically measured the resistances based on the IV slopes in the ohmic region (at current densities, equal to or below the maximum power point) and the diffusion-limited region (where voltages rapidly decrease at currents after maximum power point). These values gave estimations of R_{ohm} (IV slope in the ohmic region) and $R_{ohm}+R_{diff}$ (IV slope in the diffusion-limited region). Useful trends were extracted for $R_{ohm}+R_{diff}$, but because they were obtained from the non-linear region of the IV curve, larger error bars were typically recorded. These results were complemented by quantification of maximum power ($P0_{max}$), current at the maximum power point ($j0_{mpp}$), and maximum current ($j0_{max}$) to promote a discussion of the involved mechanisms contributing to the LSV results.

3 Results

3.1 Electrochemical performance and resistances with time

The microfluidic MFC was operated for 50 h, after which we began acquiring polarization curves using LSV (Figure 2a) and adjusting the external resistance based on the results. No overshoot was observed at any time, indicating that the EAB was not stressed by oxygen accumulation or from exposure to ferricyanide crossover from the catholyte co-flow stream. We credit this to the improved fluid delivery system, which avoided crossover of the catholyte to the anode chamber [5]. From an analysis of the polarization curves at 50 h in Figure 2a, several indicators showed that performance was improved as the EAB matured. These included continuous increases in OCV, maximum current, and maximum power densities (I_A and P_A, respectively). The internal resistances were also observed and quantified based on the IV curve slopes [36], which we mark on one curve in Figure 2a for demonstration purposes. For example, R_{ohm} was measured based on the slope at current densities associated with maximum power point, and it was found to continuously decrease based on the slope of the IV curve in the ohmic region (R_{ohm}). The observed decreases to R_{ohm} in time were likely due to decreasing charge transfer resistance as a continuous EAB layer was established on the anode surface. It should be noted that at 50 h, no stable linear ohmic region was observed in the polarization curves. The ohmic region in the polarization curves at later times is clearly observed, with the linear region extended to higher current densities at 150 h compared to 100 h (Figure 2b). We also measured the slope at high current densities after the system became diffusion limited. The slope in the second case is related to both R_{ohm} and the diffusion resistance (R_{diff}), which we label as $R_{ohm}+R_{diff}$. Plots of R_{ohm} versus time showed an initial drop of 40% was measured for R_{ohm} between 50 and 100 h, after which it remained approximately constant at 6 kΩ. However, $R_{ohm}+R_{diff}$ continued to decrease until 150 h. This reduction in resistance can be explained by the continuous reduction in the boundary layer thickness around the EAB due to increased flow velocities through the diminishing free volume surrounding the growing biofilm [37–39]. Another mechanism that might have reduced diffusion resistance could have been related to proposed forced convection through the biofilm [31,40], especially for the

head-on approach of the liquid against the biofilm growing outward from a channel surface [41]. For example, recent work showed that the EAB structural properties may change over time, resulting in a more open and permeable structure [42]. In summary, considering the continuous reduction in diffusion resistance during the experiment, it appears that the EAB continued to grow after 100 h, but this did not affect the ohmic resistance, likely because the charge transfer resistance was already at a minimum after a full biofilm monolayer was established and the increases to biofilm thickness were not enough to add measurable ohmic resistance.

Analysis of the respective power density curves (Figure 2c) revealed an expected shift of the maximum power point to higher current densities ($j0_{mpp}$), along with significant increases to maximum power density ($P0_{max}$). Specifically, the values for anode-area normalized $P0_{max}$ ($j0_{mpp}$) obtained at 50, 100 and 150 h were 0.44±0.03 (1.20±0.026), 1.018±0.14 (2.62±0.34) and 1.51±0.02 W m^{-2} (4.07±0.13) W m^{-2} (A m^{-2}), respectively. The continuous improvements to power output correlate with the aforementioned reduction in diffusion resistance. Similar trends were observed for the maximum current densities ($j0_{max}$), which were measured to be 1.92±0.03, 3.64±0.40 and 5.65±0.07 A m^{-2} at 50, 100, and 150 h, respectively. It is interesting to note that $j0_{max}$ and $P0_{max}$ appear to increase nearly linearly with time (Figure 2d). This may be because of constant accumulation of EAB thickness, which was previously noted to be proportional to EAB outputs for young biofilms [43].

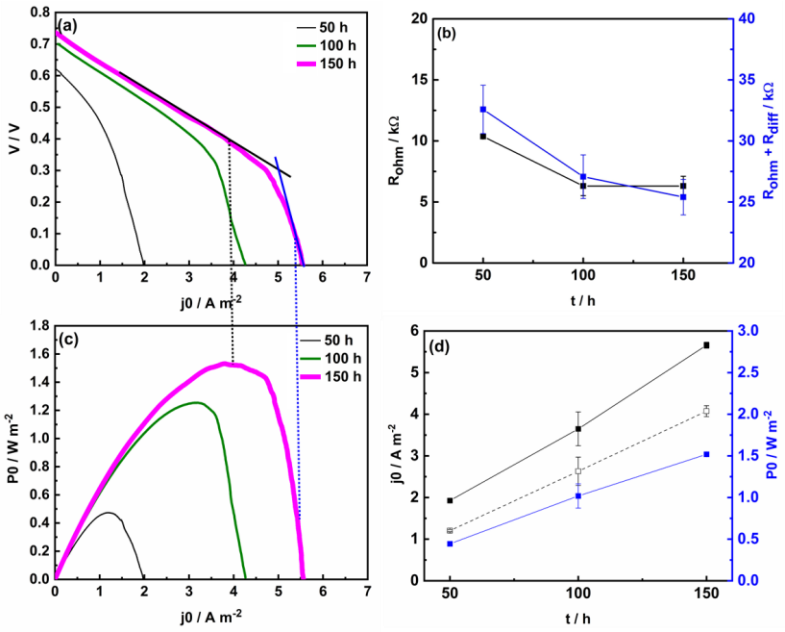

Figure 2. Electrochemical performance and resistances during 50, 100, and 150 h operation of the microfluidic MFC with total flow rate Q_T=1 mL h^{-1}. (a) Polarization (IV) curves obtained from LSV (scan rate of 1 mV s^{-1}) and (b) analysis of the slopes in the ohmic region (equivalent to R_{ohm}, black) and the diffusion-limited region (equivalent to R_{ohm}+R_{diff}, blue). Power density curves are shown in (c). Points on the 150 h power density curve exemplify the relationship between current density at which the slope on the polarization curve in (a) was measured. This includes slopes at the maximum power point (black dashed) and in the diffusion-limited region (blue dashed). Analysis of (c) is plotted as a function of time in (d), including maximum current ($j0_{max}$, black), current at maximum power point $j0_{mpp}$, (black dashed), and maximum power ($P0_{max}$, blue).

3.2 High-throughput optimization of MFC outputs by modulation of experimental conditions

After power density stabilized under the growth conditions, nearly one week later, a series of rapid optimization experiments were conducted to identify the conditions that could maximize current and power density outputs in the newly matured EAB. These experiments were only possible with the use of 4-way valves that enabled continuous bubble-free liquid delivery during syringe replacement to avoid flow disturbances, which would have otherwise made iterative optimization experiments difficult due to variations to experimental outputs.

3.2.1 Effect of total flow rate on performance and cell resistances

First, we studied the role of flow rate by imposing values ranging from Q_T=0.6 to 40 mL h^{-1} while maintaining a 1:1 flow rate ratio between the anolyte and catholyte streams. Polarization curves at different flow rates are shown in Figure 3a. Neither OCV nor R_{ohm} changed noticeably with flow rate. The latter was analysed accordingly (Figure 3b), revealing values ranging between R_{ohm}=4.77±0.05 and 5.15±0.29 kΩ, or varying by about ± 7%. This is consistent with previous studies demonstrating that flow rate does not significantly affect MFC internal resistances at or near the maximum power point for macroscale [44,45] or microfluidic MFCs [1,21]. On the other hand, analysis of R_{ohm}+R_{diff} in the diffusion-limited region showed continuous reductions from 35 to 22 kΩ while the flow rate ranged from 0.6 mL h^{-1} to 20 mL h^{-1}. As R_{ohm} is roughly constant in this range, we attribute all changes in R_{ohm}+R_{diff} at high current densities to R_{diff}, which decreases with flow-induced reductions of the boundary layer thickness [46–48]. At 30 mL h^{-1}, R_{ohm}+R_{diff} experienced a jump to approximately 45 kΩ, which we attribute to flow instability and a wandering co-flow interface. Next, we analysed the power density curves (Figure 3c) and obtained $P0_{max}$, $j0_{mpp}$, and $j0_{max}$ (Figure 3d), all of which were sensitive to flow rate. The maximum current

densities reached $j0_{max}$=6.0±0.14 A m^{-2} at 20 mL h^{-1} before decreasing at higher flow rates (30 and 40 mL h^{-1}) corresponding to the increases to R_{diff} noted above. Flow-based changes to $P0_{max}$ were also not monotonic, as increases with flow rates transitioned to reductions for flow rates greater than 15 to 20 mL h^{-1}. Some authors have previously reported loss of power and current to erosion of the EAB. Indeed, with the present electrode architecture, which places the electrodes away from slow flow in the channel corners, the average shear stresses applied to anode-adhered biofilms are expected to be high relative to other designs [49]. To test this theory, we conducted a second flow rate cycle after the first cycle (6 h). Unlike the first cycle, the second started at high flow rates. In comparing the data from the two cycles, no significant differences were observed, indicating no permanent modifications to the EAB performance over the time scale of the experiment. Since the doubling rate of *G. sulfurreducens* bacteria is about 6 hours [50], we cannot strictly rule out erosion followed by biofilm regrowth, though if this did occur, it is expected that the second cycle, which was run in reverse should have resulted in more significant differences in the results than were observed. Another explanation for the reduced power and current densities above Q=20 mL h^{-1} is the effect of reversible (elastic) deformation of the EAB [51,52]. If such deformations compressed the EAB, this could have reduced its inner pore structure, thus limiting acetate permeability into the EAB. However, recent studies show that under tangential flow mode, such deformations may actually open the EAB structure due to lift forces being generated [53,54]. Another possibility is that stretching the EAB may have reduced the EAB electrical conductivity. This may be the source of the relatively small increases in R_{ohm}, but not the relatively large increase in R_{ohm}+R_{diff}. Therefore, it is likely that the increases in R_{ohm}+R_{diff} resulted from the instability of the co-flow interface, leading to crossover to the opposite electrode chambers at high flow rates [55,56] as hypothesized above. The larger error bars at high flow rates support this hypothesis because the instability would not lead to repeatable results. We leave this question for future studies, but for now, we note that Q_T=20 mL h^{-1} produced electrode areal-normalized outputs that were only slightly improved over those obtained at 3 mL h^{-1}. Considering the improved fluid management that results in higher acetate conversion at low flow rates [5], 3 mL h^{-1} is considered an excellent option for optimized operation. We credit the lower sensitivity to flow rate originating from the optimized placement of electrodes away from the channel wall, resulting in a more uniform flow field being applied to the electrode-adhered EAB. This is in contrast to other designs which

demonstrate continuous increases to outputs up to much higher flow rates because wall-adjacent portions will experience a higher sensitivity to flow due to large gradient in flow velocities.

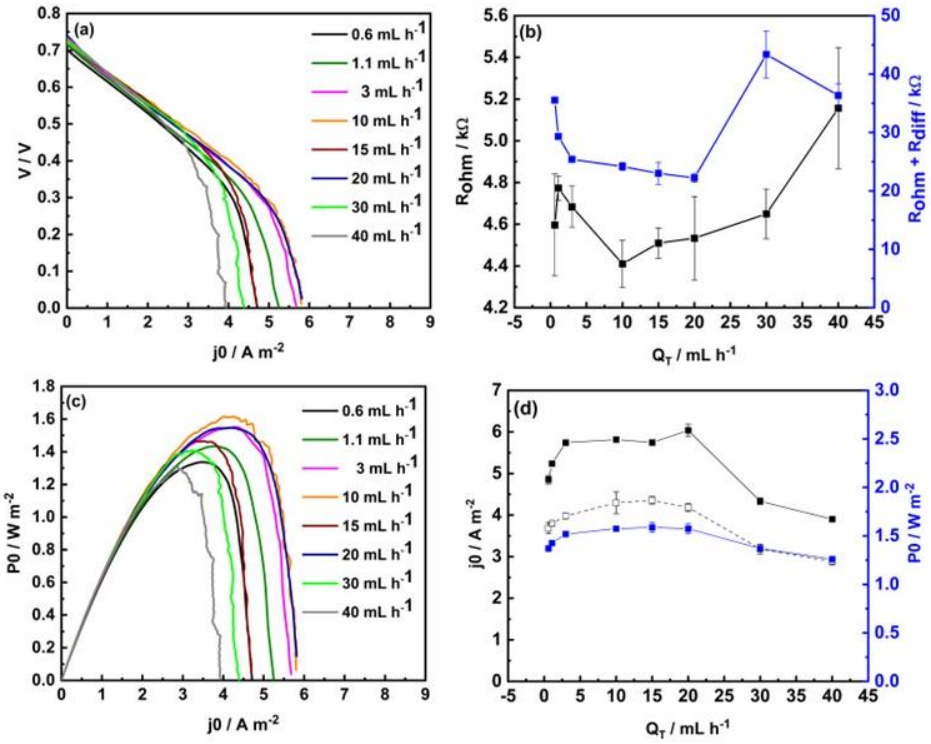

Figure 3. The electrochemical performances were evaluated at various total flow rates (Q_T) ranging from 0.6 to 40 mL h^{-1} while the anolyte and catholyte flow rates ratio were held constant at 1:1. (a) Polarization (IV) curves obtained from linear sweep voltammetry (scan rate of 1 mV s^{-1}) and (b) analysis of slopes in the ohmic region (R_{ohm}, black) and the diffusion-limited region (equivalent to R_{ohm}+R_{diff}, blue). Note the difference in scale between each y-axis. Power density curves are shown in (c), and the resistance analysis is plotted as a function of flow rate in (d), including maximum current ($j0_{max}$, black), current at maximum power point $j0_{mpp}$, (black dashed), and maximum power ($P0_{max}$, blue).

3.2.2 Effect of imbalanced flow rates on outputs and cell resistances

Membraneless microfluidic MFCs are susceptible to disturbances to the co-flow interface position due to user error, imprecise pumping, or maintenance procedures such as syringe replacement. We mimicked the effect of a wandering co-flow interface by the choice of flow rate ratio between the catholyte and anolyte flow streams (Q_C:Q_A) while keeping the total flow rate constant at 3 mL h^{-1}. The three flow rate ratios (Q_C:Q_A) were (i) 0.5:2.5, (ii) 1:2, and (iii) 1.5:1.5, with units of mL h^{-1} in all cases. For all imbalanced flow rates, we maintained flows with Q_C<Q_A to prevent contact

of ferricyanide against the EAB, which could induce hysteresis in repeat results and cause overall reductions in performance. At each flow rate condition, we calculated the polarization curves (and their corresponding power density curves) in triplicate. The average R_{ohm} and $R_{ohm}+R_{diff}$ were not significantly affected by the flow rate ratio (Figure 4a), though a balanced co-flow (Q_C:Q_A=1.5:1.5) produced the best results of $P0_{max}$=1.27±0.04 W m^{-2} and $j0_{mpp}$=3.18±0.10 A m^{-2} (Figure 4b). This may be related to the increased ionic strength in the channel, due to higher percentage of high ionic strength catholyte compared to other flow conditions. The marginal differences in outputs at each flow ratio condition suggest that low ferricyanide flow rate may be enough to support fast reaction kinetics while limiting the chance for EAB exposure to the catholyte stream to the greatest extent possible. Nevertheless, in this work, we preferred to extract the slightly improved performance from a balanced flow.

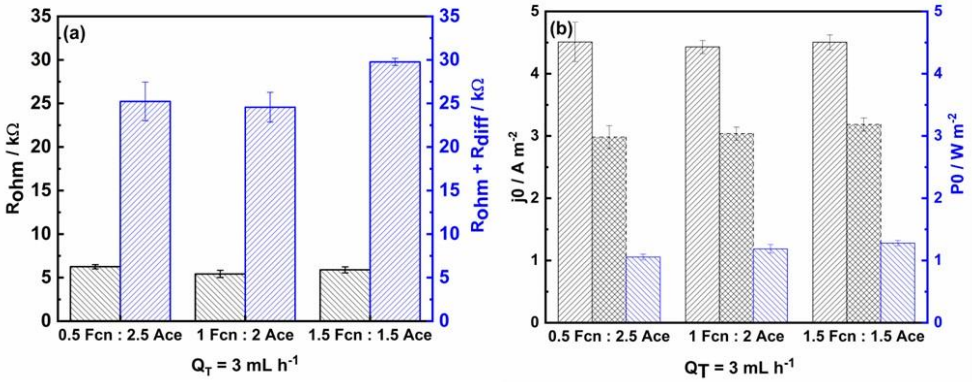

Figure 4. Electrochemical results obtained under constant total flow rate (Q_T=3 mL h^{-1}) at three flow rates ratios (Q_C:Q_A) of 0.5:2.5, 1:2, and 1.5:1.5 mL h^{-1}. (a) R_{ohm} (black) and $R_{ohm}+R_{diff}$ (blue) for the average results. (b) Maximum current density ($j0_{max}$, black diagonal), current density at maximum power point ($j0_{mpp}$, black double cross-hatch), and maximum power ($P0_{max}$, blue diagonal). The anolyte and catholyte concentrations were 10 mM and 30 mM, respectively.

3.2.3 Independent optimization of anolyte and catholyte concentrations

Generally, most MFC developers have their own anolyte and catholyte recipes. In this work, we took advantage of rapid LSV measurements while we modulated concentrations to evaluate performance in a range that covered most of those used in literature. In microfluidic MFCs, ferricyanide is generally used as a catholyte because its fast reduction can overcome kinetic limitations at the cathode, enabling a clearer evaluation of EAB performance [56,57]. As well, until reliable small-scale air cathodes are refined and transferred to microfluidic MFC architecture

[58], dissolved ferricyanide as an oxidizer remains the most practical option for this work [30]. Optimization of ferricyanide concentrations is generally not performed, probably because ferricyanide is considered to be an efficient redox molecule with fast reduction kinetics. Nevertheless, a wide range of concentrations is used in the literature, which may affect device performance and undermine comparisons between different studies. To test the effect of electron acceptor concentration on MFC performance, we applied the catholyte with ferricyanide concentrations between 1 and 130 mM while the acetate concentration was held constant at 10 mM. Polarization curves were obtained, and an analysis of the resistances was conducted (Figure 5a). A continuous near-exponential reduction in R_{ohm} from approximately 8 to 5 kΩ was observed as the ferricyanide concentration was increased from 1 to 130 mM. This result is likely due to corresponding increases in solution conductivity resulting from increased potassium and ferricyanide ions (Supplementary Information, Table S1). In the same ferricyanide concentration range, more complex changes to $R_{ohm}+R_{diff}$ were recorded, though the large error bars in the latter should be noted. Between 1 and 10 mM, $R_{ohm}+R_{diff}$ slightly decreased to approximately 23 kΩ, whereas at concentrations above 10 mM, $R_{ohm}+R_{diff}$ increased to nearly 33 kΩ. We attribute this to the oversupply of ferricyanide, which increased the kinetics to the point at which acetate became limiting at the anode.

Following the analysis of the effect of ferricyanide concentrations on performance, the MFC was left to stabilize for 24 h under 10 kΩ external resistance with 10 mM acetate and 30 mM ferricyanide while maintaining the same flow rate (Q_T=1 mL h^{-1}). Next, the acetate concentration was varied between 0.3 and 20 mM while polarization curves were generated (Figure 5b). Similar to the observed effects in response to the ferricyanide concentrations, the increasing applied acetate concentration resulted in an initial decrease to R_{ohm} at low concentrations (though the change was much less pronounced, less than 1 kΩ), followed by nearly no changes at higher acetate concentrations. Regarding the effects of diffusion, a significant decrease in $R_{ohm}+R_{diff}$ was measured from 60 to 15 kΩ as the acetate concentration was increased up to 5 mM. At higher acetate concentrations, the diffusion resistance increased, with $R_{ohm}+R_{diff}$ reaching 24 kΩ at 20 mM. We attribute this result to an oversupply of acetate, which resulted in fast kinetics, such that diffusion limitations resulted at the cathode. We note that proposed diffusion limitations at the anode and cathode, due to high concentrations of either the catholyte ferricyanide or anolyte acetate, respectively, led to increases to $R_{ohm}+R_{diff}$ of approximately 10 kΩ in both cases. However,

this effect occurred over a smaller interval for acetate (10 to 20 mM), compared to that of ferricyanide (5 to 130 mM). We attribute this to the fact that ferricyanide reduction is a one-electron process, whereas oxidation of one acetate molecule results in a reduction of 8 ferricyanide molecules, so the high current resulting from increases to acetate will deplete the ferricyanide faster than the inverse situation.

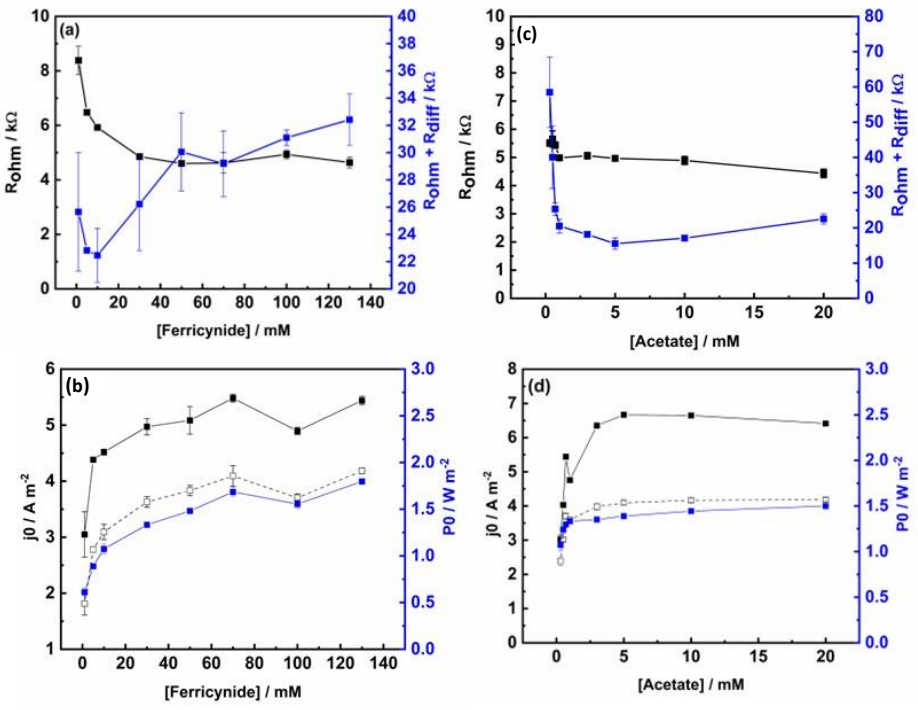

Figure 5. Electrochemical performance and figures of merit at different catholyte and anolyte concentrations. Changing ferricyanide concentrations while maintaining a 10 mM acetate concentration at the anode resulted in (a) measurements of ohmic resistance (R_{ohm}, black) and ohmic and diffusion resistance (R_{ohm}+R_{diff}, blue) and (b) maximum current ($j0_{max}$, black), current at maximum power point ($j0_{mpp}$, dashed), and maximum power ($P0_{max}$, blue). Changing acetate concentrations while holding ferricyanide constant at 30 mM at the cathode resulted in measurements of (c) ohmic resistance (R_{ohm}, black) and ohmic and diffusion resistance (R_{ohm}+R_{diff}, blue) and (d) maximum current ($j0_{max}$, black), current at maximum power point ($j0_{mpp}$, dashed), and maximum power ($P0_{max}$, blue). In all cases, total flow rate was constant at Q_T=1 mL h^{-1}.

Independent of the changing cell resistances, current and power continuously increased as more ferricyanide and acetate were added to the system (Figures 5c and 5d). These increases included a more than doubling of $j0_{mpp}$ and $j0_{max}$ when the ferricyanide concentrations were increased from 1 to 130 mM, leading to maximum values of 4.2 and 5.5 A m^{-2}, respectively. In the same concentration interval, $P0_{max}$ increased by a factor of three, leading to a maximum value of 1.8 W m^{-2}. Even higher outputs were obtained at the highest acetate concentration, leading to $j0_{mpp}$, $j0_{max}$,

and $P0_{max}$ values of 4.1 A m^{-2}, 6.75 A m^{-2}, and 1.44 W m^{-2}, respectively, at 5 mM. Increasing the acetate concentration up to 20 mM led to marginal improvements in $j0_{mpp}$ and $P0_{max}$ of 4.2 A m^{-2} and 1.5 W m^{-2}, respectively. In contrast, $j0_{max}$ decreased slightly to 6.45 A m^{-2}, suggesting that without further increases in ferricyanide to address cathode limitations, the 5 mM acetate concentration can be used as an optimal concentration at a 1 mL h^{-1} flow rate.

3.2.4 Effect of temperature on cell performance and resistances

The role of operating temperature is crucial in determining the overall MFC performance [59]. While most studies do not control the temperature, others generally maintain elevated levels near 30°C [60]. As a proof of principle, we tested 3 thermal conditions, typical (25°C), near-optimal (30°C), and overheated (35°C), to demonstrate simultaneous temperature control with LSV measurements and the related analysis (Figures 6a and 6b). As expected, the current and power densities were optimal at 30°C. An exact optimal value is not sought in this work, but this can easily be determined with finer adjustments to the temperature. Though 35°C performed better than 25°C, outputs were worse than at 30°C, and prolonged exposure to high temperatures can result in heat damage, which can cause long-term deficiencies in the MFC [59]. It has been shown that the R_{ohm} resistance is also strongly dependent on the temperature [60]. This dependence is observed in the current work, with R_{ohm} decreasing from 5.99±0.04 kΩ (25°C) to 4.83±0.13 kΩ (30°C), after which it maintained stability up to 35°C. This observation is interesting because the electrical resistivity of direct metal-like conductors, such as electrodes, generally increases with temperature. The decrease in ohmic resistance may be related to the improved metabolism at elevated temperatures, indicating a biological aspect to the ohmic resistance. For example, the biofilm/electrode interface layer may maintain better contact at optimal temperatures, or some other aspect of cellular electron transfer could be improved. Unsurprisingly, the resistance in the current-limited region ($R_{ohm}+R_{diff}$) showed improvements with temperature, decreasing linearly at approximately 1.5 kΩ K^{-1}, likely due to the related improvements in diffusional mass transport. Despite improvements in resistance at 35°C, an analysis of power density curves (Figure 6c) revealed a decline in current and power density in the same interval (Figure 6d). The maximum current and power densities peaked at 4.1 A m^{-2} and 2.5 W m^{-2}, respectively, at 30°C, but decreased by about 10% at 35°C, likely due to heat-related reductions in bacterial metabolism. In summary, we used LSV to detect the MFC response while temperature was accurately controlled and other

conditions were precisely maintained. Among the temperatures used, 30ºC produced the best results.

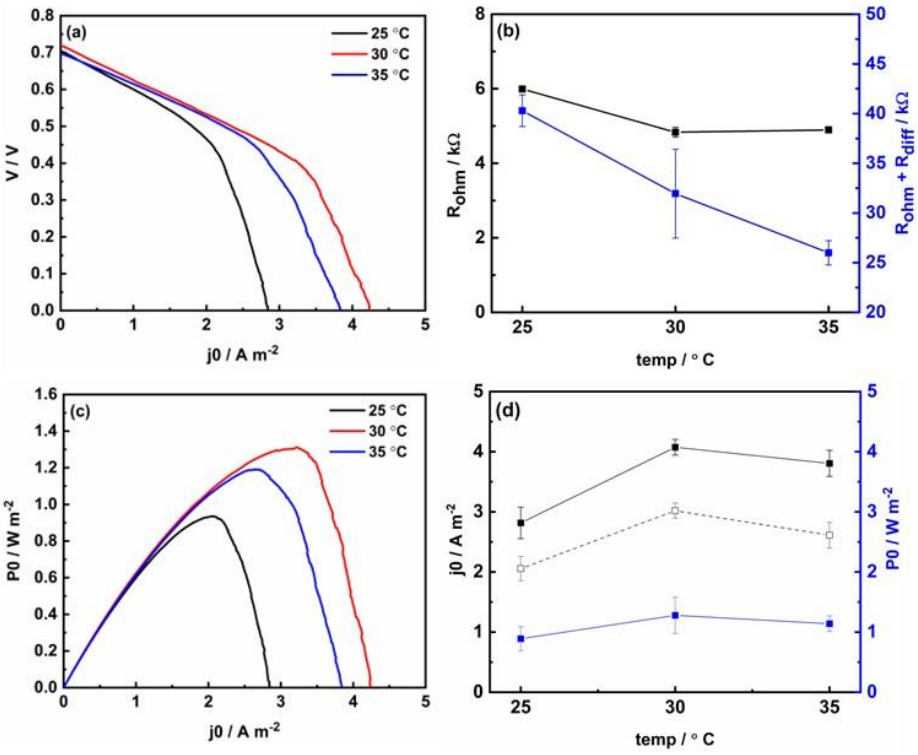

Figure 6. Electrochemical performance and changes in resistances as a function of operating temperature. (a) Polarization (IV) curves obtained from LSV (scan rate of 1 mV s^{-1}) and (b) analysis of slopes in the ohmic region (equivalent to R_{ohm}, black) and the diffusion-limited region (equivalent to $R_{ohm}+R_{diff}$, blue). Power density curves are shown in (c), and the analysis is plotted as a function of temperature (d), including maximum current ($j0_{max}$, black), current at the maximum power point $j0_{mpp}$ (black dashed), and maximum power ($P0_{max}$, blue). In all experiments, the flow rate was constant at Q_T=1 mL h^{-1}.

3.3 MFC operation under optimized conditions

After determination of each individual optimized parameter, we combined the best conditions to observe their combined effects. These values are shown in Table 1 for total flow rate, flow rate ratio, concentrations (ferricyanide and acetate), and temperature. In the cases in which the optimal values did not yield significantly different outputs than those with more onerous conditions (higher flow rates, higher concentrations), we chose different options. For example, as discussed above, the advantages of a lower total flow rate at Q_T=3 mL h^{-1} outweigh slightly improved currents at Q_T=20 mL h^{-1}.

Table 1. Optimal experimental conditions.

Experimental parameter	Optimal value	Set value	R_{ohm} (kΩ)	$P0_{max}$ (W m^{-2})	$j0_{max}$ (A m^{-2})
Total flow rate, Q_T	20 mL h^{-1}	3 mL h^{-1}	4.53±0.19	1.57±0.05	6.03±0.14
Flow rate ratio, Q_C:Q_A	1:1	1:1	5.89±0.34	1.27±0.04	4.50±0.12
[Ferricyanide]	130 mM	70 mM	4.63±0.20	1.79±0.02	5.43±0.07
[Acetate]	10 mM	10 mM	4.43±0.14	1.50±0.01	6.41±0.02
Temperature	30°C	30°C	4.83±0.13	1.27±0.02	4.07±0.10

One day after the experimental parameters were changed to the set values noted in Table 1, we re-set the experimental clock at t=0, which corresponded to approximately 2 weeks of operation prior to optimizing all experimental parameters. Then we undertook electrochemical measurements, with the results given in Figure 7a. Immediately following t=0, the synergetic effect of all conditions applied together resulted in improvements in power and current, which became higher than any of the individual results observed in the preceding experiments. The improvements to $j0_{max}$ were particularly impressive, increasing by nearly 30% over the highest maximum current obtained from the optimization of any singular variable to 8.3 A m^{-2}. Similarly, there was an immediate but modest (9%) increase in $P0_{max}$ to 1.95 W m^{-2} over the best value obtained in the previous section. After 2 days of operation under optimized experimental conditions, improvements in polarization and power density curves continued as the EAB successfully adapted to its new conditions (Figure 7a). The changes to maximum power density, current density, and current density at the maximum power point obtained on day 0 and day 2 after switching to optimized conditions are shown in Figure 7b. At day 2, these values had increased to $P0_{max}$=2.48±0.10 W m^{-2} and $j0_{max}$=10.49±0.83 A m^{-2}. These values mark improvements of 27% and 26.5% over the t=0 values and 38.5% and 63.7% over the best values obtained for the best single optimized parameter.

The synergistic effect of all optimized conditions also lowered the values of R_{ohm} and R_{ohm}+R_{diff}, relative to measurements made earlier in this work (Figure 7c). This shift was marginal for R_{ohm}, which was reduced to 2.69±0.30 kΩ on day 2 from its day 0 value of 3.35±0.24 kΩ. The strongest

changes occurred in the resistances under diffusion-limited conditions, which were reduced to $R_{ohm}+R_{diff}$=11.68±1.10 kΩ at day 2 from $R_{ohm}+R_{diff}$=18.90±1.22 kΩ at day 0. These findings emphasize the importance of extended operation for the microfluidic MFC under optimized conditions.

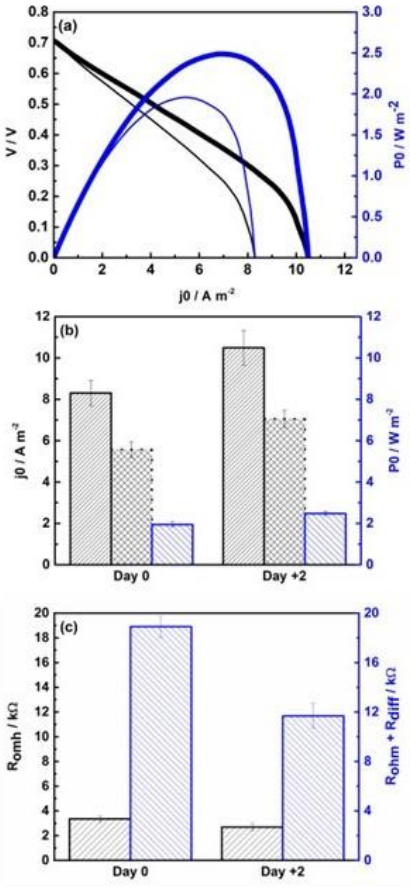

Figure 7. Electrochemical performance of the microfluidic microbial fuel cell under optimized conditions at day 0 and day 2. (a) Current-voltage characteristic of the device; Q_T was 3 mL h^{-1}. (b) $P_{max,}$ $j0_{max}$ and $j0_{max}$ at maximum power point. (c) R_{ohm} and $R_{ohm}+R_{diff}$.

4 Discussion and conclusions

We demonstrate microfluidic MFCs to explore the operational parameter space as a useful application for the precision experimental control afforded within microchannels. Following the identification of optimal conditions during the parameter sweep, we observed that the simultaneous application of all optimal parameters at the same time resulted in MFC regrowth, leading to further improvements. The final maximum power density ($P0_{max}$=2.48±0.10 W m^{-2}) and particularly the current density ($j0_{max}$=10.49±0.83 A m^{-2}), based on projected anode area, were among the highest

anode-area normalized outputs to date for a microfluidic MFC. The reader is directed to Table 2, where we compare our results to other notable microfluidic MFC results. The normalized power densities may be significantly higher than reported above. While normalizing by projected electrode area is typical in microfluidic MFCs literature, we have recently shown that not all of the electrode surface area is useful for EAB growth in side-by-side electrodes [5]. Rather, as previous authors have demonstrated, outputs can be limited by bottlenecks in the electrolyte contact area between the anode and cathode chambers [32,33]. Considering this fact, we previously determined that the normalized high-power densities of a well-performing microfluidic MFC could reach 8.1 W m^{-2} [5]. Applying the same approach to the present results, we normalized the results by the cross-sectional area ($A_{x\text{-}sec}$), which is 6.05 times smaller than the projected anode area (see experimental section), resulting in maximum power and current densities of $P0_{max}^{x-sec}$=15.0 W m^{-2} and $j0_{max}^{x-sec}$=63.46 A m^{-2}. The former approaches the theoretical limit calculated as between 17 and 19 W m^{-2} [61]. Owing to the astonishing differences in output densities calculated by this approach, in comparison to those calculated from projected area reported in the literature, further investigation is necessary to explore this approach.

Finally, further refinements of this approach are merited since the optimal conditions for any one parameter may change based on values of the other parameters, an iterative optimization process should be applied. For example, increases high diffusion resistance which is observed when the concentration of one chamber are increased to the point of severe stoichiometric imbalance points concentration increases to the opposite chamber as an avenue to further improve performance. This concept is at the heart of so-called self-driving labs, which not only have the potential to modify reaction conditions but, via closed-loop monitoring of outputs, can also optimize the conditions on the fly using a combination of automated lab equipment and artificial intelligence [62]. Considering the ease in tracking MFC outputs with excellent time and signal resolution, along with highly controllable experimental parameters on-chip, automated liquid delivery systems [63] and embedded controllable heating elements [64,65], it is possible that microfluidic MFCs can be excellent candidates for extended work that follows a self-optimizing route. Indeed, the initial work into automated algorithms already includes automated power harvesting [66] and machine learning for microfluidic MFC design [67] and predictive self-optimizing algorithms [68]. Thus, the future direction of this work should aim for a fully automated system that can push the limits of MFC optimization, potentially redefining the role of microfluidic MFCs. This can be coupled

with innovations in microfabrication [73] and integration of other analytical tools, such as Fourier transform infrared spectroscopy [74,75,76], Raman spectroscopy [77], and microfluidic analytical methods to study biofilms [78] to gain more information on the EAB during modulations of experimental parameters.

Table 2. Comparison of notable microfluidic MFC outputs.

Year	Cell type	[Acetate] (mM)	[Ferricyanide] (mM)	Q_T (mL h^{-1})	Temp. (°C)	R_{int} (Ω)	I_{max} (A m^{-2})	P_A (W m^{-2})	P_v^{**} (kWm^{-3})	Ref
2013	Membraneless (mixed culture)	10	20	20	25	2.35	2.2	0.618	0.618	[56]
2013	Membrane (CEM) (mixed culture)	20	100	0.12	30	10k	2.14	0.95	6.129	[57]
2015	Membraneless (mixed culture)	40	30	40	RT	NA	10.5	2.447	2.178	[69]
2016	Membraneless (mixed culture)	40	30	40	NA	1092	7.8	1.810	1.810	[70]
2016	Membrane (mixed culture)	10	50	3.84	40	NA	6.06	2.460	4.920	[71]
2018	Membraneless (mixed culture)	10	50	1.2	35	NA	1.82	0.719	7.189	[72]
2021	Membraneless (*G. sulfurreducens*)	10	30	140	23	25k	1.04	0.456	0.356	[4]

2022	Membrane (porous) (*G. sulfurreducens*)	10	30	10	23	10k	3.54	0.660	4.4	[1]
2023	Membraneless (*G. sulfurreducens*)	10	30	100	23	NA	8.50	3.884	24.37	[5]
2023	Membraneless (*G. sulfurreducens*)	10	70	3	30	NA	10.49	2.48	15.63	Present work

■ Acknowledgements

The authors acknowledge financial support from Sentinelle Nord and the Natural Sciences and Engineering Research Council of Canada. They also thank M. K. Gregas for technical edits.

■ Declaration of Competing Interest

The authors declare that they have no known competing financial interests or personal relationships that could have influenced the work reported in this paper.

References

[1] L. Gong, M. Abbaszadeh Amirdehi, J.M. Sonawane, N. Jia, L. Torres de Oliveira, J. Greener, Mainstreaming microfluidic microbial fuel cells: a biocompatible membrane grown in situ improves performance and versatility, Lab Chip. 22 (2022) 1905–1916. https://doi.org/10.1039/d2lc00098a.

[2] J.M. Sonawane, S.A. Patil, P.C. Ghosh, S.B. Adeloju, Low-cost stainless-steel wool anodes modified with polyaniline and polypyrrole for high-performance microbial fuel cells, J Power Sources. 379 (2018) 103–114. https://doi.org/10.1016/j.jpowsour.2018.01.001.

[3] J.M. Sonawane, R. Mahadevan, A. Pandey, J. Greener, Recent progress in microbial fuel cells using substrates from diverse sources, Heliyon. 8 (2022) e12353. https://doi.org/10.1016/j.heliyon.2022.e12353.

[4] M.A. Amirdehi, N. Khodaparastasgarabad, H. Landari, M.P. Zarabadi, A. Miled, J. Greener, A High-Performance Membraneless Microfluidic Microbial Fuel Cell for Stable, Long-Term Benchtop Operation Under Strong Flow, ChemElectroChem. 7 (2020) 2227–2235. https://doi.org/10.1002/CELC.202000040.

[5] N. Khodaparastasgarabad, J.M. Sonawane, H. Baghernavehsi, L. Gong, L. Liu, J. Greener, Microfluidic membraneless microbial fuel cells: new protocols for record power densities, Lab Chip. 23 (2023) 4201–4212. https://doi.org/10.1039/D3LC00387F.

[6] I. Ieropoulos, J. Winfield, J. Greenman, Effects of flow-rate, inoculum and time on the internal resistance of microbial fuel cells, Bioresour Technol. 101 (2010) 3520–3525. https://doi.org/10.1016/j.biortech.2009.12.108.

[7] J. Winfield, I. Ieropoulos, J. Greenman, J. Dennis, Investigating the effects of fluidic connection between microbial fuel cells, Bioprocess Biosyst Eng. 34 (2011) 477–484. https://doi.org/10.1007/s00449-010-0491-x.

[8] R. Rossi, D. Pant, B.E. Logan, Chronoamperometry and linear sweep voltammetry reveals the adverse impact of high carbonate buffer concentrations on anode performance in microbial fuel cells, J Power Sources. 476 (2020) 228715. https://doi.org/10.1016/j.jpowsour.2020.228715.

[9] A.R. Rahmani, N. Navidjouy, M. Rahimnejad, S. Alizadeh, M.R. Samarghandi, D. Nematollahi, Effect of different concentrations of substrate in microbial fuel cells toward bioenergy recovery and simultaneous wastewater treatment, Environmental Technology (United Kingdom). 43 (2022) 1–9. https://doi.org/10.1080/09593330.2020.1772374.

[10] G.M. Tardy, B. Lóránt, M. Lóka, Substrate concentration dependence of voltage and power production characteristics in two-chambered mediator-less microbial fuel cells with acetate and peptone substrates, Biotechnol Lett. 39 (2017) 383–389. https://doi.org/10.1007/s10529-016-2256-3.

[11] D. Ucar, Y. Zhang, I. Angelidaki, An overview of electron acceptors in microbial fuel cells, Front Microbiol. 8 (2017) 643. https://doi.org/10.3389/fmicb.2017.00643.

[12] K. Lawson, R. Rossi, J.M. Regan, B.E. Logan, Impact of cathodic electron acceptor on microbial fuel cell internal resistance, Bioresour Technol. 316 (2020) 123919. https://doi.org/10.1016/j.biortech.2020.123919.

[13] M. Aghababaie, M. Farhadian, A. Jeihanipour, D. Biria, Effective factors on the performance of microbial fuel cells in wastewater treatment–a review, Environmental Technology Reviews. 4 (2015) 71–89. https://doi.org/10.1080/09593330.2015.1077896.

[14] P. Sobieszuk, A. Zamojska-Jaroszewicz, Ł. Makowski, Influence of the operational parameters on bioelectricity generation in continuous microbial fuel cell, experimental and computational fluid dynamics modelling, J Power Sources. 371 (2017) 178–187. https://doi.org/10.1016/j.jpowsour.2017.10.032.

[15] S. Gadkari, J.M. Fontmorin, E. Yu, J. Sadhukhan, Influence of temperature and other system parameters on microbial fuel cell performance: Numerical and experimental investigation, Chemical Engineering Journal. 388 (2020) 124176. https://doi.org/10.1016/j.cej.2020.124176.

[16] H. Ren, C. Jiang, J. Chae, Effect of temperature on a miniaturized microbial fuel cell (MFC), Micro and Nano Systems Letters. 5 (2017) 1–7. https://doi.org/10.1186/s40486-017-0048-8.

[17] L. Gong, M. Abbaszadeh Amirdehi, A. Miled, J. Greener, Practical increases in power output from soil-based microbial fuel cells under dynamic temperature variations, Sustain Energy Fuels. 5 (2021) 671–677. https://doi.org/10.1039/d0se01406k.

[18] T. Ouyang, X. Hu, W. Liu, X. Shi, J. Lu, An innovative model for biofilm-based microfluidic microbial fuel cells, J Power Sources. 521 (2022) 230940. https://doi.org/10.1016/J.JPOWSOUR.2021.230940.

[19] T.A. Duncombe, A.M. Tentori, A.E. Herr, Microfluidics: Reframing biological enquiry, Nat Rev Mol Cell Biol. 16 (2015) 554–567. https://doi.org/10.1038/nrm4041.

[20] Y. Zhang, R.R. Xiao, T. Yin, W. Zou, Y. Tang, J. Ding, J. Yang, Generation of gradients on a microfluidic device: Toward a high-Throughput investigation of spermatozoa chemotaxis, PLoS One. 10 (2015) e0142555. https://doi.org/10.1371/journal.pone.0142555.

[21] M.A. Amirdehi, L. Gong, N. Khodaparastasgarabad, J.M. Sonawane, B.E. Logan, J. Greener, Hydrodynamic interventions and measurement protocols to quantify and mitigate power overshoot in microbial fuel cells

using microfluidics, Electrochim Acta. 405 (2022) 139771. https://doi.org/10.1016/J.ELECTACTA.2021.139771.

[22] V. Miralles, A. Huerre, F. Malloggi, M.C. Jullien, A review of heating and temperature control in microfluidic systems: Techniques and applications, Diagnostics. 3 (2013) 33–67. https://doi.org/10.3390/diagnostics3010033.

[23] F. Zhao, R.C.T. Slade, J.R. Varcoe, Techniques for the study and development of microbial fuel cells: An electrochemical perspective, Chem Soc Rev. 38 (2009) 1926–1939. https://doi.org/10.1039/b819866g.

[24] M. Shirkosh, Y. Hojjat, M.M. Mardanpour, Boosting microfluidic microbial fuel cells performance via investigating electron transfer mechanisms, metal-based electrodes, and magnetic field effect, Scientific Reports 2022 12:1. 12 (2022) 1–16. https://doi.org/10.1038/s41598-022-11472-6.

[25] M.P. Zarabadi, S.J. Charette, J. Greener, Flow-Based Deacidification of Geobacter sulfurreducens Biofilms Depends on Nutrient Conditions: a Microfluidic Bioelectrochemical Study, ChemElectroChem. 5 (2018) 3645–3653. https://doi.org/10.1002/celc.201800968.

[26] S. Pinck, L.M. Ostormujof, S. Teychené, B. Erable, Microfluidic microbial bioelectrochemical systems: An integrated investigation platform for a more fundamental understanding of electroactive bacterial biofilms, Microorganisms. 8 (2020) 1–22. https://doi.org/10.3390/microorganisms8111841.

[27] J. Wang, R. Polsky, B. Tian, M.P. Chatrathi, Voltammetry on microfluidic chip platforms, Anal Chem. 72 (2000) 5285–5289. https://doi.org/10.1021/ac000484h.

[28] T.C. Dang, Y. Yin, Y. Yu, D.T. Phan, C. Yang, B. Cao, H. Song, Y. Kang, A membrane-free micro-fluidic microbial fuel cell for rapid characterization of exoelectrogenic bacteria, Microfluid Nanofluidics. 20 (2016) 1–8. https://doi.org/10.1007/s10404-016-1811-5.

[29] S. Srikanth, J.M. Mohan, S. Raut, S.K. Dubey, I. Ishii, A. Javed, S. Goel, Droplet based microfluidic device integrated with ink jet printed three electrode system for electrochemical detection of ascorbic acid, Sens Actuators A Phys. 325 (2021) 112685. https://doi.org/10.1016/j.sna.2021.112685.

[30] Y. Yang, D. Ye, J. Li, X. Zhu, Q. Liao, B. Zhang, Microfluidic microbial fuel cells: From membrane to membrane free, J Power Sources. 324 (2016) 113–125. https://doi.org/10.1016/j.jpowsour.2016.05.078.

[31] L. Gong, N. Khodaparastasgarabad, D.M. Hall, J. Greener, A new angle to control concentration profiles at electroactive biofilm interfaces: Investigating a microfluidic perpendicular flow approach, Electrochim Acta. 431 (2022) 141071. https://doi.org/10.1016/J.ELECTACTA.2022.141071.

[32] R. Rossi, B.E. Logan, Using an anion exchange membrane for effective hydroxide ion transport enables high power densities in microbial fuel cells, Chemical Engineering Journal. 422 (2021) 130150. https://doi.org/10.1016/j.cej.2021.130150.

[33] R. Rossi, B.E. Logan, Unraveling the contributions of internal resistance components in two-chamber microbial fuel cells using the electrode potential slope analysis, Electrochim Acta. 348 (2020) 136291. https://doi.org/10.1016/J.ELECTACTA.2020.136291.

[34] S.B. Velasquez-Orta, T.P. Curtis, B.E. Logan, Energy from algae using microbial fuel cells, Biotechnol Bioeng. 103 (2009) 1068–1076. https://doi.org/10.1002/bit.22346.

[35] J. Winfield, I. Ieropoulos, J. Greenman, J. Dennis, The overshoot phenomenon as a function of internal resistance in microbial fuel cells, Bioelectrochemistry. 81 (2011) 22–27. https://doi.org/10.1016/j.bioelechem.2011.01.001.

[36] B.E. Logan, Microbial Fuel Cells | Wiley, 2008.

[37] M.P. Gashti, J. Bellavance, O. Kroukamp, G. Wolfaardt, S.M. Taghavi, J. Greener, Live-streaming: Time-lapse video evidence of novel streamer formation mechanism and varying viscosity, Biomicrofluidics. 9 (2015) 041101. https://doi.org/10.1063/1.4928296.

[38] J. Kim, H.S. Kim, S. Han, J.Y. Lee, J.E. Oh, S. Chung, H.D. Park, Hydrodynamic effects on bacterial biofilm development in a microfluidic environment, Lab Chip. 13 (2013) 1846–1849. https://doi.org/10.1039/c3lc40802g.

[39] P.L. Bishop, J.T. Gibbs, B.E. Cunningham, Relationship between concentration and hydrodynamic boundary layers over biofilms, Environmental Technology (United Kingdom). 18 (1997) 375–385. https://doi.org/10.1080/09593331808616551.

[40] M.P. Zarabadi, M. Couture, S.J. Charette, J. Greener, A Generalized Kinetic Framework Applied to Whole-Cell Bioelectrocatalysis in Bioflow Reactors Clarifies Performance Enhancements for Geobacter Sulfurreducens Biofilms, ChemElectroChem. 6 (2019) 2715–2718. https://doi.org/10.1002/celc.201900732.

[41] H.J. Eberl, C. Picioreanu, J.J. Heijnen, M.C.M. Van Loosdrecht, Three-dimensional numerical study on the correlation of spatial structure, hydrodynamic conditions, and mass transfer and conversion in biofilms, Chem Eng Sci. 55 (2000) 6209–6222. https://doi.org/10.1016/S0009-2509(00)00169-X.

[42] J., Z.M.P., H.D.M., D.S., G.J., Y.L. Zhao, Unification of cell-scale metabolic activity with biofilm behavior by integrating advanced flow and reactive-transport modeling and microfluidic experiments, Energy & Environmental Science, Submitted . (2023).

[43] D.R. Bond, D.E. Holmes, L.M. Tender, D.R. Lovley, Electrode-reducing microorganisms that harvest energy from marine sediments, Science (1979). 295 (2002) 483–485. https://doi.org/10.1126/science.1066771.

[44] N.A. ElNaker, A.F. Yousef, S.W. Hasan, Effect of hydraulic retention time on microbial community structure in wastewater treatment electro-bioreactors, Microbiologyopen. 7 (2018). https://doi.org/10.1002/mbo3.590.

[45] G. Liu, M.D. Yates, S. Cheng, D.F. Call, D. Sun, B.E. Logan, Examination of microbial fuel cell start-up times with domestic wastewater and additional amendments, Bioresour Technol. 102 (2011) 7301–7306. https://doi.org/10.1016/J.BIORTECH.2011.04.087.

[46] P. Perrodin, C. Sella, L. Thouin, Electrochemical Generation of Steady-State Linear Concentration Gradients within Microfluidic Channels Perpendicular to the Flow Field, Anal Chem. 92 (2020) 7699–7707. https://doi.org/10.1021/acs.analchem.0c00645.

[47] W. Rösing, T. Schildhauer, J. König, C. Cierpka, Passive control of the concentration boundary layer in microfluidic fuel cells using Dean vortices, Microfluid Nanofluidics. 23 (2019) 1–11. https://doi.org/10.1007/s10404-019-2274-2.

[48] S.K. Yoon, G.W. Fichtl, P.J.A. Kenis, Active control of the depletion boundary layers in microfluidic electrochemical reactors, Lab Chip. 6 (2006) 1516–1524. https://doi.org/10.1039/b609289f.

[49] F. Asayesh, M.P. Zarabadi, N.B. Aznaveh, J. Greener, Microfluidic flow confinement to avoid chemotaxis-based upstream growth in a biofilm flow cell reactor, Analytical Methods. 10 (2018) 4579–4587. https://doi.org/10.1039/c8ay01513a.

[50] D.R. Lovley, E.J.P. Phillips, Novel mode of microbial energy metabolism: organic carbon oxidation coupled to dissimilatory reduction of iron or manganese, Appl Environ Microbiol. 54 (1988) 1472–1480. https://doi.org/10.1128/aem.54.6.1472-1480.1988.

[51] H. Nguyen, A. Ybarra, H. Başağaoğlu, O. Shindell, Biofilm viscoelasticity and nutrient source location control biofilm growth rate, migration rate, and morphology in shear flow, Scientific Reports 2021 11:1. 11 (2021) 1–17. https://doi.org/10.1038/s41598-021-95542-1.

[52] E.S. Gloag, G.K. German, P. Stoodley, D.J. Wozniak, Viscoelastic properties of Pseudomonas aeruginosa variant biofilms, Scientific Reports 2018 8:1. 8 (2018) 1–11. https://doi.org/10.1038/s41598-018-28009-5.

[53] M.C.J.G. N. Khodaparastasgarabad, A kinetic study on the transduction of chemical concentrations into electrical current in a microfluidic bioelectrochemical device, Submitted. (n.d.).

[54] C. Picioreanu, F. Blauert, H. Horn, M. Wagner, Determination of mechanical properties of biofilms by modelling the deformation measured using optical coherence tomography, Water Res. 145 (2018) 588–598. https://doi.org/10.1016/J.WATRES.2018.08.070.

[55] E.R. Choban, L.J. Markoski, A. Wieckowski, P.J.A. Kenis, Microfluidic fuel cell based on laminar flow, J Power Sources. 128 (2004) 54–60. https://doi.org/10.1016/j.jpowsour.2003.11.052.

[56] D. Ye, Y. Yang, J. Li, X. Zhu, Q. Liao, B. Deng, R. Chen, Performance of a microfluidic microbial fuel cell based on graphite electrodes, in: Int J Hydrogen Energy, Pergamon, 2013: pp. 15710–15715. https://doi.org/10.1016/j.ijhydene.2013.05.034.

[57] S. Choi, J. Chae, Optimal biofilm formation and power generation in a micro-sized microbial fuel cell (MFC), Sens Actuators A Phys. 195 (2013) 206–212. https://doi.org/10.1016/J.SNA.2012.07.015.

[58] M. Di Lorenzo, A.R. Thomson, K. Schneider, P.J. Cameron, I. Ieropoulos, A small-scale air-cathode microbial fuel cell for on-line monitoring of water quality, Biosens Bioelectron. 62 (2014) 182–188. https://doi.org/10.1016/J.BIOS.2014.06.050.

[59] L.H. Li, Y.M. Sun, Z.H. Yuan, X.Y. Kong, Y. Li, Effect of temperature change on power generation of microbial fuel cell, Https://Doi-Org.Acces.Bibl.Ulaval.ca/10.1080/09593330.2013.828101. 34 (2013) 1929–1934. https://doi.org/10.1080/09593330.2013.828101.

[60] K.C. Obileke, H. Onyeaka, E.L. Meyer, N. Nwokolo, Microbial fuel cells, a renewable energy technology for bio-electricity generation: A mini-review, Electrochem Commun. 125 (2021) 107003. https://doi.org/10.1016/J.ELECOM.2021.107003.

[61] B.E. Logan, Exoelectrogenic bacteria that power microbial fuel cells, Nat Rev Microbiol. 7 (2009) 375–381. https://doi.org/10.1038/nrmicro2113.

[62] M. Abolhasani, E. Kumacheva, The rise of self-driving labs in chemical and materials sciences, Nature Synthesis 2023 2:6. 2 (2023) 483–492. https://doi.org/10.1038/s44160-022-00231-0.

[63] F. Kong, L. Yuan, Y.F. Zheng, W. Chen, Automatic liquid handling for life science: a critical review of the current state of the art, J Lab Autom. 17 (2012) 169–185. https://doi.org/10.1177/2211068211435302.

[64] A.A. Dos-Reis-Delgado, A. Carmona-Dominguez, G. Sosa-Avalos, I.H. Jimenez-Saaib, K.E. Villegas-Cantu, R.C. Gallo-Villanueva, V.H. Perez-Gonzalez, Recent advances and challenges in temperature monitoring and control in microfluidic devices, Electrophoresis. 44 (2023) 268–297. https://doi.org/10.1002/ELPS.202200162.

[65] V. Miralles, A. Huerre, F. Malloggi, M.C. Jullien, A Review of Heating and Temperature Control in Microfluidic Systems: Techniques and Applications, Diagnostics. 3 (2013) 33. https://doi.org/10.3390/DIAGNOSTICS3010033.

[66] H. Wang, J. Do Park, Z.J. Ren, Practical energy harvesting for microbial fuel cells: A review, Environ Sci Technol. 49 (2015) 3267–3277. https://doi.org/10.1021/ES5047765/ASSET/IMAGES/ES-2014-047765_M003.GIF.

[67] D.D. Nguyen, T. Quy Duc Pham, M. Tanveer, H. Khan, J.W. Park, C.W. Park, G.M. Kim, Deep learning–based optimization of a microfluidic membraneless fuel cell for maximum power density via data-driven three-dimensional multiphysics simulation, Bioresour Technol. 348 (2022) 126794. https://doi.org/10.1016/J.BIORTECH.2022.126794.

[68] D.D. Nguyen, M. Tanveer, H.N. Mai, T.Q.D. Pham, H. Khan, C.W. Park, G.M. Kim, Guiding the optimization of membraneless microfluidic fuel cells via explainable artificial intelligence: Comparative analyses of multiple machine learning models and investigation of key operating parameters, Fuel. 349 (2023) 128742. https://doi.org/10.1016/J.FUEL.2023.128742.

[69] Y. Yang, D. Ye, J. Li, X. Zhu, Q. Liao, B. Zhang, Biofilm distribution and performance of microfluidic microbial fuel cells with different microchannel geometries, in: Int J Hydrogen Energy, Pergamon, 2015: pp. 11983–11988. https://doi.org/10.1016/j.ijhydene.2015.04.144.

[70] Y. Yang, D. Ye, Q. Liao, P. Zhang, X. Zhu, J. Li, Q. Fu, Enhanced biofilm distribution and cell performance of microfluidic microbial fuel cells with multiple anolyte inlets, Biosens Bioelectron. 79 (2016) 406–410. https://doi.org/10.1016/j.bios.2015.12.067.

[71] H. Ren, H. Tian, C.L. Gardner, T.L. Ren, J. Chae, A miniaturized microbial fuel cell with three-dimensional graphene macroporous scaffold anode demonstrating a record power density of over 10000 W m-3, Nanoscale. 8 (2016) 3539–3547. https://doi.org/10.1039/c5nr07267k.

[72] J.Y. Yoon, Y. Ahn, U. Schröder, Parylene C-coated PDMS-based microfluidic microbial fuel cells with low oxygen permeability, J Power Sources. 398 (2018) 209–214. https://doi.org/10.1016/j.jpowsour.2018.07.064.

[73] G. Wegner, N. Allard, A. Al Shboul, M. Auger, et al. Functional materials: For energy, sustainable development and biomedical sciences, Walter de Gruyter GmbH & Co KG, Chapter 14, 375-410.

[74] N. Jia, A. Daignault-Bouchard, T. Deng, T. G. Mayerhöfer, A. Bégin-Drolet, J. Greener, SpectIR-fluidics: completely customizable microfluidic cartridges for high sensitivity on-chip infrared spectroscopy with point-of-application studies on bacterial biofilms, Lab Chip, 23 (2023) 3561-3570

[75] N. Jia, L. Torres de Oliveira, A. Bégin-Drolet , J. Greener, A spectIR-fluidic reactor for monitoring fast chemical reaction kinetics with on-chip attenuated total reflection Fourier transform infrared spectroscopy, Anal Methods, 15 (2023) 5129-5138.

[76] M. Pousti, M. Joly, P. Roberge, M.A. Abbaszadeh, A. Begin-Drolet, J. Greener, Linear scanning ATR-FTIR for chemical mapping and high-throughput studies of Pseudomonas sp. biofilms in microfluidic channels, Anal. Chem., 90 (2018) 14475–14483.

[77] F. Paquet-Mercier, N. B. Aznaveh, M. Safdar, J. Greener, A Microfluidic Bioreactor with in situ SERS Imaging for the Study of Controlled Flow Patterns of Biofilm Precursor Materials, Sensors, 13 (2013) 14714-14727.

[78] M. Pousti, M. P. Zarabadi, M. A. Amirdehi, F. Paquet-Mercier, J. Greener, Microfluidic bioanalytical flow cells for biofilm studies: a review, Analyst, 144 (2019) 68-86.